



## Research paper

## Reconstructing porous media using generative flow networks

Kelly M. Guan<sup>a</sup>, Timothy I. Anderson<sup>b</sup>, Patrice Creux<sup>c</sup>, Anthony R. Kovscek<sup>a,\*</sup><sup>a</sup> Stanford University, Energy Resources Engineering Department, 367 Panama St, Stanford, CA 94305-2220, USA<sup>b</sup> Stanford University, Electrical Engineering Department, 350 Jane Stanford Way, Stanford, CA 94305-9505, USA<sup>c</sup> Université de Pau et des Pays de l'Adour, E2S UPPA, CNRS, TOTAL, LFCR, Pau, France

## ARTICLE INFO

## Keywords:

Image analysis

Sandstone

Machine learning

Deep learning

## ABSTRACT

One area of intense scientific interest for the study of sandstones, carbonates, and shale at the pore scale is the use of limited image and petrophysical data to generate multiple realizations of a rock's pore structure. Such images aid efforts to quantify uncertainty in petrophysical properties, including porosity–permeability transforms. We develop and evaluate a deep learning-based method to synthesize porous media volumes using a so-called generative flow model trained on x-ray microscope images of rock texture and pore structure. These models are optimized on a log-likelihood objective and they synthesize large and realistic three-dimensional images. We demonstrate the rapid generation of sandstone image volumes that display realism as gauged by quantitative comparison of topological features using Minkowski functionals of porosity, specific surface area, and the Euler–Poincaré characteristic (i.e., pore connectivity). We also evaluate the single-phase permeability using Navier–Stokes and lattice Boltzmann methods and show that transport properties of the generated samples match measured trends.

## 1. Introduction

Understanding fluid flow in porous media at the micro-scale is relevant to many fields, such as oil and gas recovery, geothermal energy, geological CO<sub>2</sub> storage, and battery energy storage. Porous medium properties, such as porosity and permeability, are often calculated from laboratory measurements or direct imaging of the microstructure (Walsh and Frangos, 1968; Ketcham and Carlson, 2001; Josh et al., 2012; Callow et al., 2020). Due to acquisition times and experimental costs, however, it is difficult to evaluate the variability of these properties across multiple macroscopic samples especially as sample permeability decreases. Instead, researchers often use statistical methods to reconstruct porous media based on either two-point or multi-point statistics (Okabe and Blunt, 2007; Wang et al., 2018). Reconstruction using these methods often requires prior knowledge about the pore- and throat-size distributions and can be time-consuming to generate multiple realizations of the same rock sample.

Various methods are available to reconstruct porous media, such as simulated annealing and multi-point statistical (MPS) methods. Simulated annealing can incorporate multiple correlation functions and statistical properties during reconstruction (Yeong and Torquato, 1998; Manwart et al., 2000; Pant and Berkeley, 2016). The method has been used to generate 2D and 3D Fontainebleau and Berea sandstone structures but can take hours to days to create large volumes (Manwart

et al., 2000; Čapek et al., 2009; Pant and Berkeley, 2016). Extensions of the simulated annealing technique have also been used to generate multi-scale heterogeneous materials from multiple data sources, as well as generating 3D binary volumes from limited, multimodal data (Chen et al., 2016; Li et al., 2018). MPS techniques have been used to reconstruct large-scale reservoir systems, as well as micro-scale porous media, but also are slow to scale to generate multiple, large volumes (Caers, 2001; Okabe and Blunt, 2004, 2007; Bai and Tahmasebi, 2020). Pattern-based MPS methods have allowed for faster reconstruction of 3D networks using a cross-correlation based simulation method (CCSIM), but MPS techniques still struggle to capture long-range connectivity (Tahmasebi et al., 2012, 2014, 2017). Other recent methods for reconstructing three-dimensional porous volumes include texture synthesis and gradient-based methods as well (Liu and Shapiro, 2015; Fullwood et al., 2008).

Given the multi-scale nature of many rock systems, an ideal reconstruction method is one that recreates different length scales accurately and rapidly from a few datasets and is equally applicable to conventional and unconventional porous media. Recently, advances in machine learning, specifically in generative modeling, have focused on learning from limited datasets and generalizing these learned features for various applications (Goodfellow et al., 2014; Dinh et al., 2015; Zhu et al., 2017).

\* Corresponding author.

E-mail addresses: [kmguan@stanford.edu](mailto:kmguan@stanford.edu) (K.M. Guan), [timothy.anderson@stanford.edu](mailto:timothy.anderson@stanford.edu) (T.I. Anderson), [patrice.creux@univ-pau.fr](mailto:patrice.creux@univ-pau.fr) (P. Creux), [kovscek@stanford.edu](mailto:kovscek@stanford.edu) (A.R. Kovscek).<https://doi.org/10.1016/j.cageo.2021.104905>

Received 31 October 2020; Received in revised form 26 July 2021; Accepted 2 August 2021

Available online 8 August 2021

0098-3004/© 2021 Elsevier Ltd. All rights reserved.

The major contribution of this work is the application of generative flow models to 3D volumes of porous media exhibiting grains, pore throats, and pore bodies. The advantage of this method is that the training is done on 2D grayscale images. The training time and model size are reduced, thereby improving scalability of the algorithm for training on larger image sizes. We generate 3D grayscale images via a latent space interpolation using a modifiable Gaussian distribution. The volumes generated are shown to be as useful as the original datasets for computing porosity, permeability, mercury injection capillary pressure, and other rock properties. We verify the accuracy of the generated images by calculating morphological parameters and comparing them against the real rock dataset. Accordingly, this paper proceeds by proposing implementation of generative flow models, metrics for evaluating the accuracy of model results, computation of permeability from 3D images, discussing results, and then conclusions.

## 2. Generative models

Deep-learning generative modeling is classified into two main approaches: generative adversarial networks (GANs) and likelihood-based methods. GANs are composed of two networks, a generator and discriminator, that work in competition against one another (Goodfellow et al., 2014). The generator attempts to recreate the training image as realistically as possible in order to fool the discriminator, that attempts to discern between a real or fake image. Deep convolutional GANs (DCGANs) are a class of GANs that use a convolutional neural network (CNNs) architecture in the generator and discriminator (Radford et al., 2015). CNNs are well-suited for image-based deep learning tasks, but must be trained on a fixed image size for a given network.

The second type of generative model, likelihood-based methods, is comprised of three groups: autoregressive models, variational autoencoders, and flow-based generative models. Each method has their advantages and disadvantages. Autoregressive models are simple to train but difficult to parallelize on larger image sizes (Hochreiter and Schmidhuber, 1997; Graves, 2013). Variational autoencoders are more parallelizable and optimize the lower bound of the log-likelihood of data (Kingma and Dhariwal, 2018). However, they can be difficult to optimize. Finally, flow-based generative models are a more recent technique that use a series of invertible transformations to yield a model with a tractable density function (Dinh et al., 2015, 2017).

### 2.1. Application to geological sciences

Generative models have been used in geosciences for inverse modeling and history matching of reservoirs and reconstruction of image volumes before (Chan and Elsheikh, 2019; Mosser et al., 2020; Krutko et al., 2019; Wang et al., 2020; Volkhonskiy et al., 2019; Anderson et al., 2020b). Most researchers have focused on using GANs to recreate porous media images. Often, these GANs are coupled with additional parameters or autoencoders to improve image quality by introducing more information or limitations (Feng et al., 2019; Volkhonskiy et al., 2019; Fokina et al., 2020). Advantages of using GANs over stochastic methods described earlier are rapid generation of the images, especially in 3D, and removing the necessity of incorporating physical parameters that must be predetermined from the rock dataset. One disadvantage of GANs, however, is that the training image size is often fixed and dependent on the CNN architecture. In order to train on larger image volumes, an additional layer in the generator and discriminator must be added and can make the training and optimization of the model more difficult. As a consequence, scaling the network to generate larger volumes that may be necessary to capture multi-scale features in a sample can be difficult if the training size is not large enough. Later work applied conditional and spatial transform networks to improve image quality and scalability of the output image (Uzunova et al., 2019; Mosser et al., 2018).

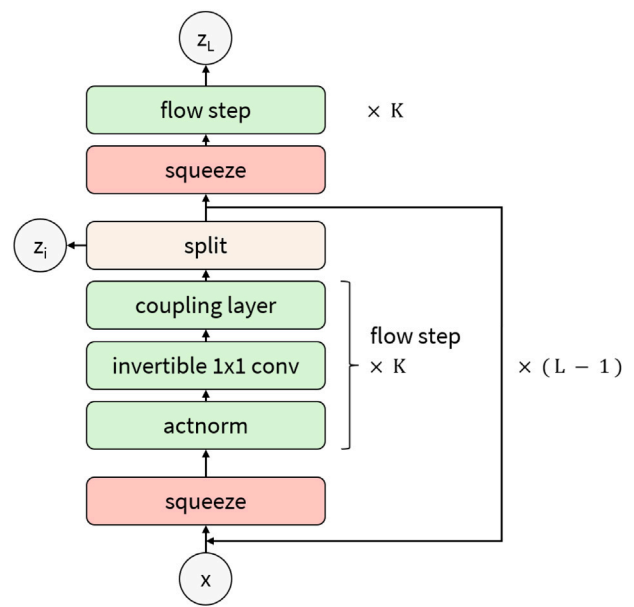


**Fig. 1.** Generative flow model architecture. The flow step is comprised of three parts: an actnorm, then an invertible  $1 \times 1$  convolution, and then a coupling layer.  $K$  is the depth of flow and  $L$  is the number of levels.  $\mathbf{x}$  is a random vector with distribution  $\mathbf{x} \sim p^*(\mathbf{x})$ , and  $\mathbf{z}$  is the latent variable.

Source: Adapted from [Kingma and Dhariwal \(2018\)](#).

There has been little work using other generative models to create synthetic rock volumes, and this is an active area of research. The assumptions concerning the regular structure of synthetic samples and the required computational time are the most limiting criteria. In this project, we aim to explore other methods for generating realistic, scalable rock samples. Specifically, we consider flow-based models due to the model’s scalability and invertability (Papamakarios et al., 2019; Kingma and Dhariwal, 2018).

### 3. Methods

The main contribution of this work is to present and evaluate a generative flow model to synthesize 3D porous media images and evaluate a series of domain-specific metrics to verify model accuracy. We demonstrate the applicability of the generative flow method using a sandstone dataset because data is widely available and petrophysical properties are fairly well-understood. We first present the generative flow model and interpolation technique, described in further detail in [Anderson et al. \(2020a\)](#) that was used on shale fabric, not granular images. Next, we detail the morphological and petrophysical evaluation metrics used to compare the real and synthetic datasets.

### 3.1. Generative flow model

We adapt a pre-existing generative model on our dataset to confirm the feasibility of this approach. Specifically, we start with a generative flow model with invertible  $1 \times 1$  convolutions, coined *Glow*, that has been shown to create realistic-looking, large images (Kingma and Dhariwal, 2018). This work is built upon the NICE and RealNVP generative models (Dinh et al., 2015, 2017).

Flow-based models use a likelihood-based objective. For the *Glow* model, this is equivalent to minimizing the negative log-likelihood of the datapoints  $\mathbf{x}$

$$\mathcal{L}(\mathcal{D}) = \frac{1}{N} \sum_{i=1}^N -\log p_{\theta}(\mathbf{x}^{(i)}) \quad (1)$$

**Table 1**  
Normalized flow model architecture and parameters.

Image size	128 <sup>2</sup> pixels
Batch size	4
Learning rate, $\alpha$	$5 \times 10^{-4}$
Warm up <sup>a</sup>	5 epochs
Epochs	30
Flow coupling	Additive

<sup>a</sup>Refers to number of epochs to warm up learning rate from 0 to  $\alpha$ .

where  $\mathcal{L}$  is the likelihood,  $\mathbf{x}$  is a random vector with distribution  $\mathbf{x} \sim p^*(\mathbf{x})$ ,  $D$  is the dataset, and  $p_\theta(\mathbf{x})$  is a model with parameters  $\theta$ . *Glow* models the datapoints  $\mathbf{x}$  as

$$\mathbf{z} \sim p(\mathbf{z}) \quad (2)$$

$$\mathbf{x} = \mathbf{g}_\theta(\mathbf{z}) \quad (3)$$

where  $\mathbf{z}$  is the latent variable and  $p(\mathbf{z})$  has a known density function, often chosen to be a Gaussian distribution,  $p(\mathbf{z}) = \mathcal{N}(\boldsymbol{\mu}, \boldsymbol{\Sigma})$ . Furthermore,  $\mathbf{g}_\theta(\cdot)$  is invertible, allowing for latent variable inference,  $\mathbf{z} = \mathbf{f}_\theta(\mathbf{x}) = \mathbf{g}_\theta^{-1}(\mathbf{x})$ . Using the change of variables formula, the log-likelihood becomes

$$\log p_\theta(\mathbf{x}) = \log p_\theta(\mathbf{z}) + \sum_{i=1}^K \log |\det(dh_i/dh_{i-1})| \quad (4)$$

where  $h_0 \equiv \mathbf{x}$  and  $h_K \equiv \mathbf{z}$ . The model architecture is shown in Fig. 1, with the flow step broken up into an actnorm (activation normalization) layer, then an invertible convolution, and finally an affine or additive transformation layer. Further details of the normalizing flow derivation and flow layers are described in Kingma and Dhariwal (2018).

Given the availability of already-implemented flow-based methods, we start with a Pytorch implementation of the original *Glow* model (van Amersfoort, 2019). We modify the code to load and process our own rock datasets and generate 3D volumes. The model is also configurable to allow for tuning of relevant hyperparameters, such as learning rate, flow coupling type, and number of channels. We use the default parameters for initial training as detailed in Table 1.

### 3.1.1. Volume generation

After the model is trained on the 2D image dataset, we generate a series of anchor slices with predetermined latent space vectors, and interpolate between the anchor slices to create the 3D volume. The interpolation is performed by taking an affine combination of the latent space representation of each anchor slice. The full sequence of latent vectors is then evaluated to create a sequence of  $x - y$  slices, and the slices stacked to form the final image volumes. Further details on the calculation of the latent vectors and generation of the image volume are described in Anderson et al. (2020a).

While it would be possible to calculate the number of interpolation steps by minimizing the negative log-likelihood of the generated images across the three Cartesian planes – assuming that the sample volume is isotropic and homogeneous – this method is time-intensive when evaluating over a large range of possible interpolation steps. Instead, we use the average pore chord length, calculated from the two-point correlation function across the  $x - y$  directions, to inform the appropriate step size in the  $z$  direction. This method allows for a hybrid approach of using statistical properties to inform the final 3D reconstruction of images that were trained via a deep-learning method.

This volume generation approach carries several advantages for scalability of model training and image volume generation. The memory savings from training on only 2D images instead of 3D volumes allows for training with higher-resolution images, images with larger fields of view, or larger batch sizes. Furthermore, all  $x - y$  slices can be evaluated in parallel, leading to  $\mathcal{O}(1)$  scaling for volume generation.

This is in contrast to previously proposed methods based on GANs that scale as  $\mathcal{O}(N)$  with the generated image volume size (Mosser et al., 2017). A drawback to the method used here is that the size of the generated images is fixed in the  $x - y$  dimensions. Unlike with GAN-based models, the network used in a generative flow model is not fully convolutional, so the network is only able to invert latent vectors of a fixed dimension. Any scaling therefore will only take place in the  $z$ -direction.

## 3.2. Evaluation metrics

### 3.2.1. Morphological parameters

To evaluate the accuracy of our model, we use a set of morphological descriptors known as Minkowski functionals. Minkowski functionals are stereological estimators providing local and global morphological information that is related to single-phase flow mechanisms (Mecke and Arns, 2005; Arns et al., 2010). In 3D, there are four Minkowski functionals that describe the geometric parameters of a set  $X$  with a smooth surface  $\partial X$ : volume  $V(X)$ , surface area  $S(X)$ , integral of mean curvature  $b(X)$ , and Euler–Poincaré characteristic  $\chi(X)$

$$V(X) = \int_X dx \quad (5)$$

$$S(X) = \int_{\partial X} dx \quad (6)$$

$$b(X) = \frac{1}{2\pi} \int_{\partial X} \frac{\kappa_1(x) + \kappa_2(x)}{2} dx \quad (7)$$

$$\chi(X) = \frac{1}{4\pi} \int_{\partial X} \kappa_1(x)\kappa_2(x) dx \quad (8)$$

where  $\kappa(x)$  is the curvature corresponding to the maximum and minimum curvature radii,  $\kappa(x) = \frac{1}{r(x)}$ .

For discrete images, the functionals are estimated using the *MorphoLibJ* library in ImageJ (Legland et al., 0000; Doube et al., 2010). The volume is determined directly by counting the number of voxels that belong to the phase of interest. From this, we divide the pore volume,  $V_{pore}$ , by the total volume,  $V_{total}$ , to obtain the porosity.

The surface area is estimated using the Crofton formula, that takes a set of lines with varying orientations and counts the number of intersections with the region of interest (Serra et al., 1982; Legland et al., 2007). We consider the intersections with pixels that are labeled as pores. The surface area is normalized against the total volume to obtain the specific surface area.

The mean breadth is measured from the Crofton formula as well and is proportional to the integral of the mean curvature (Serra et al., 1982; Ohser and Schloditz, 2009). The mean breadth is related to the tortuosity and is indicative of the resistance to flow in tubular networks (Barbosa et al., 2019).

Finally, the Euler–Poincaré characteristic in 3D describes the connectivity of the volume and is calculated as the sum of the number of vertices, edges, faces, and solids using a 6-adjacency system that considers only neighbors in the three primary directions.

$$\chi = n_{vertices} - n_{edges} + n_{faces} - n_{solids} \quad (9)$$

For a pore network, a region with a positive Euler–Poincaré characteristic has more connected solid regions than holes (pores) indicating small pore connectivity across the area. A region with a negative Euler–Poincaré characteristic has more holes and therefore a large pore connectivity across the area that can allow for fluid flow.

Finally, we compute the two-point correlation function, or covariance, of the 3D volume. The two-point correlation function has been used to inform the reconstruction of homogeneous, single-scale media (Jiao et al., 2008). For a binary image, the two-point correlation function represents the probability that two points separated by a lag distance,  $\mathbf{r}$ , are the same phase. We calculate the directional and

radially-averaged correlation function for the pore phase,  $P$ , using the following

$$S_2(\mathbf{r}) = \mathbf{P}(\mathbf{x} \in P, \mathbf{x} + \mathbf{r} \in P) \quad (10)$$

We also determine the average chord length for the pore and solid phases from the slope of two-point correlation function at the origin (Torquato, 2005)

$$\bar{l}_c^{pore} = -\frac{\phi}{S'_2(0)} \quad (11)$$

$$\bar{l}_c^{solid} = -\frac{1-\phi}{S'_2(0)} \quad (12)$$

The chord is the length between intersections of a line with the pore solid interface. The chord length is especially interesting to address heterogeneous pore structures because it provides a measure of structural disorder.

### 3.2.2. Flow parameters

In addition to porosity, the effective permeability of porous rocks depends on pore size, pore geometry, connectivity, and tortuosity of flow paths. The presence of heterogeneities (such as fissures or clay deposition) can induce preferential flow directions, so that when viewed as a continuum the flow properties could exhibit strong anisotropy.

We calculate the single-phase permeability of the generated 3D volumes and the real training dataset using identical methods. Single-phase flow in porous media is described by the Stokes equation at the pore scale (Bear, 1972). For steady state, incompressible flow, assuming no gravity effects, the conservation and momentum equations are

$$\nabla \cdot \mathbf{u} = 0 \quad (13)$$

$$\nu \Delta \mathbf{u} = \nabla P \quad (14)$$

where  $\mathbf{u}$  is the velocity field at each grid cell,  $\nabla P$  is the pressure gradient, and  $\nu$  is the kinematic viscosity. At the macro-scale, this is volume-averaged and rewritten as Darcy's law to calculate the permeability of the whole system (Whitaker, 1986). The z-component of the permeability tensor is written as

$$k_z = \frac{\nu Q}{\nabla P A_{xy}} \quad (15)$$

where  $Q$  is the integrated velocity field across a slice with area  $A_{xy}$ . We use OpenFOAM to solve the incompressible Navier–Stokes equation (Weller et al., 1998). Further details of the modeling parameters are described in Guan et al. (2019).

We also calculate the permeability using a Lattice Boltzmann (LBM) method to compare against direct numerical solutions in OpenFOAM. The Lattice Boltzmann Method considers flows to be composed of a collection of pseudo-particles that are represented by a velocity distribution function. From a computational point of view, the LBM is hyperbolic and can be solved locally, explicitly, and efficiently on massively parallelized computers (Crouse et al., 2016; Wang and Aryana, 2020).

We also obtain the pore-size distribution (PSD) directly from the synthetic and training image volumes. The PSD measures the sizes of pore volumes within the imposed resolution of the images of interest. The PSD is characteristic of the microtomographic measurements and the size reflects all the parts of the system contained in the image.

Finally, we model the mercury injection capillary pressure (MICP) process as a drainage along the vertical axis from the bottom to the top with a constant contact angle. The MICP process provides a distribution of the pressure–volume relationship when invading mercury in a porous medium. Capillary forces inhibit entry of the mercury into the pore volume. Therefore, mercury intrusion only progresses after applying a sufficiently high pressure to overcome the forces required to fill the pore throats and subsequent pores. The accepted view for this procedure is that MICP detects successive sequences of invaded pore

throats for each pressure step. The physical result is a transformation of pressure steps to pore throat size. The pore system is modeled as a series of interconnected, cylindrical tubes (Washburn, 1921). We obtain the pore throat-size distribution via these geometrical and connectivity assumptions.

MICP gives information about the succession of invaded throats and their size distribution in the porous medium. Therefore, the drainage of a rock sample provides information that may be used to determine the petrophysical transition zones via a scaling of interfacial tension and contact angle. The MICP method employs the area equivalent diameter of a circle, and consequently provides no information concerning the real pore geometry. To summarize, the pore-size distribution of the imaged rock volume provides access to the whole pore space geometry at a given resolution and MICP is an indicator of drained fluid in a connected pore space environment from one face to the opposite.

## 4. Dataset

The sandstone sample is 3 mm in diameter and 1 cm long. Although small, the sample provides significant information about the micro-structure of complex porous media at an optimal image resolution for sandstones. The dataset was obtained from micro-X-ray tomography scans of a Bentheimer sandstone core. This acquisition method produces a 3D volume depicting the rock interior in grayscale values. The full dataset dimensions are  $1024^3$  voxels with a voxel size of  $1.53 \mu\text{m}$ . In order for the 2D training image to capture an adequate area, the image was downsampled to  $256^3$  voxels with a voxel size of  $6.12 \mu\text{m}$ .

For the generative flow model, 10 000 2D images were randomly sampled from the 3D image stack for each training session. The model allows us to adjust the image size. The primary constraint is GPU memory when training on larger images and that is somewhat mitigated by decreasing the batch size. We train on  $128^2$  patches to test scalability, as shown in the results. The 3D volumes are then generated using the trained model, filtered using a  $r = 1$  spherical median kernel, and binarized using Otsu thresholding in ImageJ. The binarized volumes are used as inputs for morphological and petrophysical calculations and compared against the real, binarized dataset.

## 5. Results

The progress of training is presented first. This is followed by results for pore morphology and petrophysical results, primarily permeability and porosity.

### 5.1. Training results

We present first the loss function of the model during training. Fig. 2 shows the loss function and output images, respectively, during training the model on  $128 \times 128$  pixel images. We observe a quick drop in training loss during the first 10k iterations and then little change after 25k iterations. The generated images at different iteration steps show the evolution of the model as it learns to generate the rock images. We observe a noticeable change from 500 to 25k iterations, but afterwards there is little visual difference. This suggests that we can stop training much earlier, or that we may need to adjust the learning rate and other parameters. The generated images are comparable visually to the real training set images, and further investigation of the morphological properties is performed to verify statistical agreement with the original dataset.



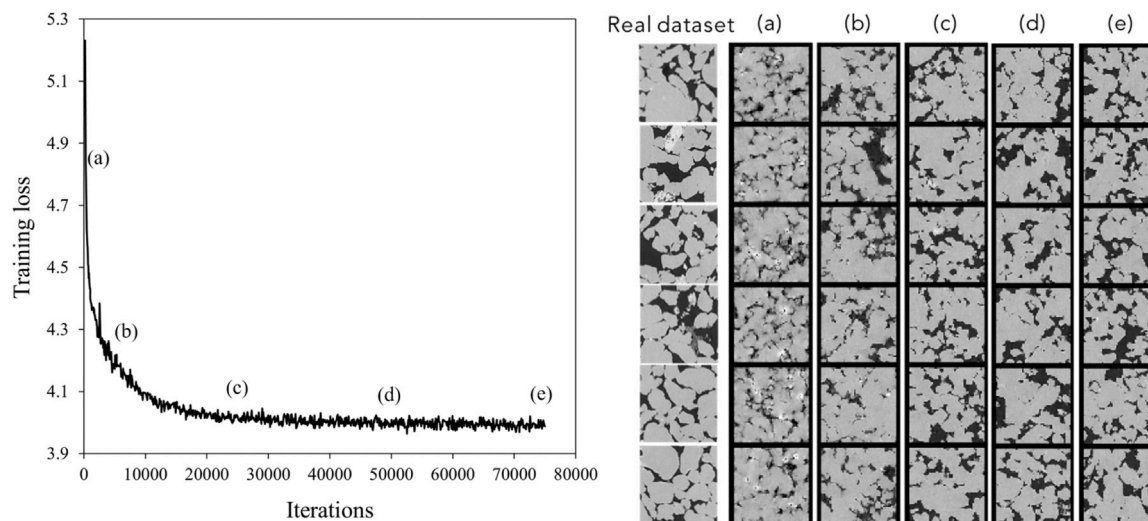


**Fig. 2.** Left: Training loss curve for the generative flow model. Training image size =  $128 \times 128$  pixels, batch size = 4, learning rate = 0.0005, number of epochs = 30, flow coupling = additive. Right: Sample of the  $128 \times 128$  training image dataset (first column) compared against outputs of the model during training. Column labels (a)–(e) correspond to iterations 500, 5000, 25 000, 50 000, and 75 000, as marked on the training loss curve.

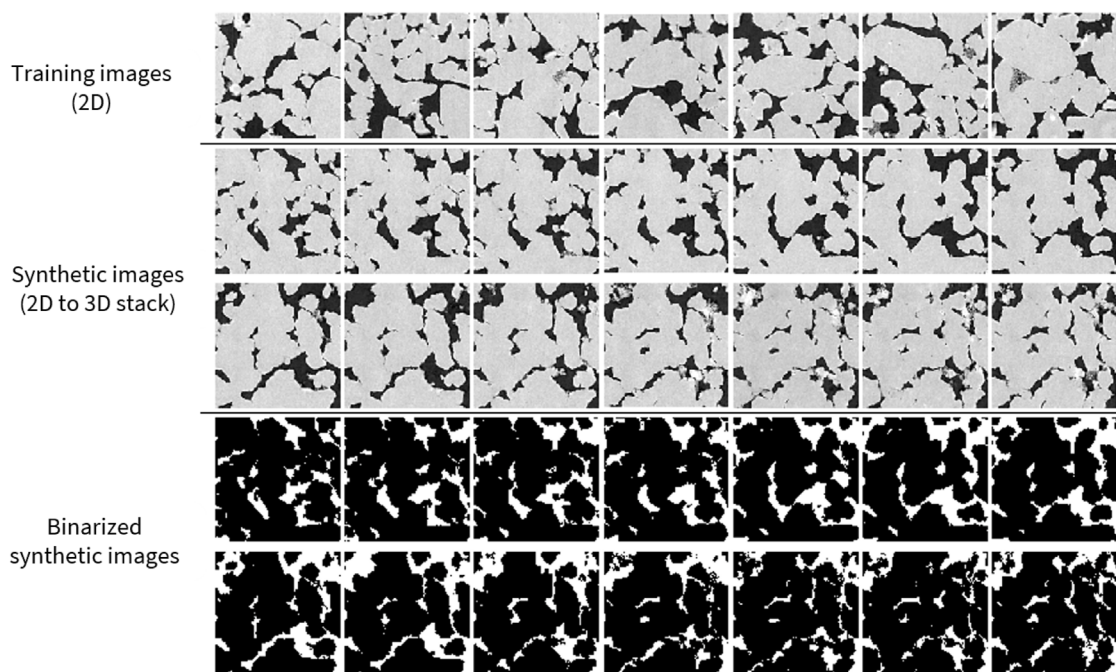


**Fig. 3.** Example of random training image slices (top) and generated image stacks (middle). The first and last generated images are anchor images and the 12 images in between are interpolated via an affine transformation of the latent space representation. The generated images are grayscale initially and then thresholded to yield a binary image stack (bottom).

## 5.2. Morphology

Fig. 3 shows an example of the training image, generated image stack, and binarized image stack. The first and last images of the synthetic 3D series are anchor images generated from the trained model. The 12 images in between are interpolated using the volume generation method described earlier. We observe in both the grayscale and binarized images that connection of the grain and pore phases is successful throughout the image stack.

Fig. 4 shows the effect of modifying the interpolation step size on the directional covariance in the interpolation plane ( $x$ -direction). We observe the best match between the training and synthetic dataset at a step size of 12 interpolated images. At a step size of 16, the

covariance at short lag distance diverges. At step sizes of 8 and 4, the covariance exhibits periodic patterns that are not in the training dataset and do not match the original dataset at short lag distances either. For the remaining results, we use a step size of 12. The directional and radially-averaged covariance for this step size is shown in Fig. 5 and indicates that the generated images capture the two-point statistics in all directions reasonably well. We observe some edge effects after 110 voxels that been observed with GAN-generated images as well, and can be resolved by cropping the image accordingly (Mosser et al., 2017).

The radially-averaged covariance of the training and synthetic data confirms agreement between the two datasets. Both training and synthetic datasets show exponential decay and stabilization at a lag distance of approximately 25 voxels. For the generated samples, the chord

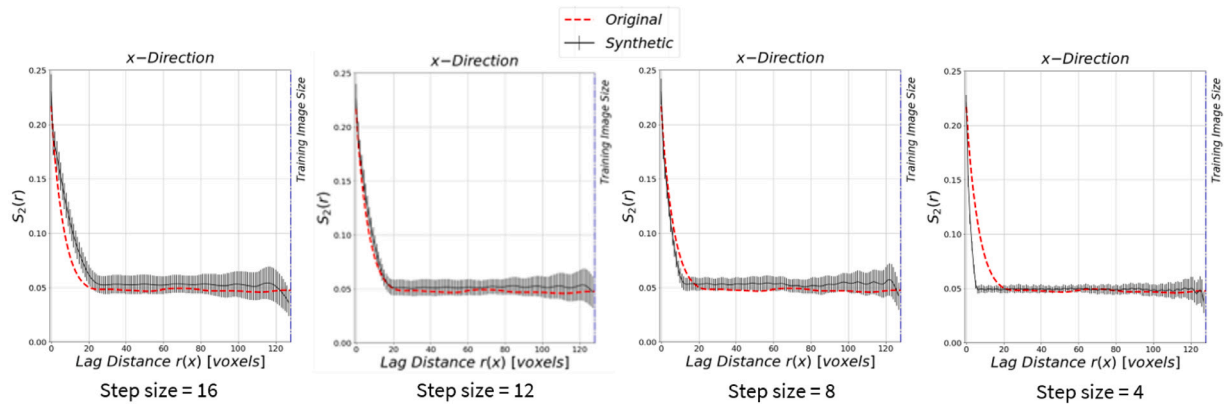


Fig. 4. Non-centered covariance of the sandstone compared against the synthetic volume in the interpolating direction (x-direction) for different interpolation step sizes. A step size of 12 shows the best agreement with the non-centered covariance of the training dataset.

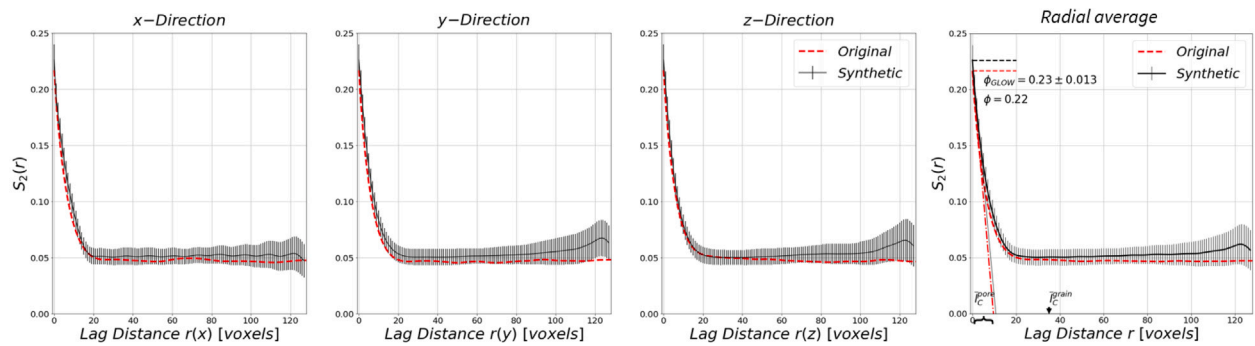


Fig. 5. Directional and radial non-centered covariance of the sandstone training image and synthetic volumes (step size = 12). The chord length of the pore and grain phases are 11 and 37 voxels, respectively.

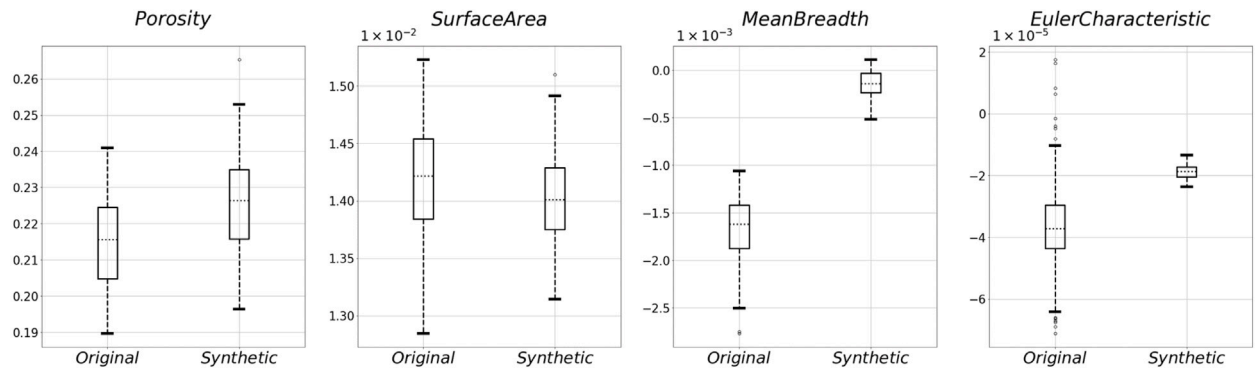


Fig. 6. Minkowski functionals – porosity, specific surface area, mean breadth, and Euler–Poincaré characteristic – for the training image set and generated images. The values and error range are similar and show good agreement between the two datasets, except for mean breadth.

length for the pore and solid phases are 11 and 37 voxels, respectively. The similarity between the chord length of the pore phase and the optimal interpolation step size further motivates using the statistical properties of the material to inform the volume generation process.

The morphological parameters calculated for the training data and synthetic data are shown in Fig. 6. The distribution of porosity, specific surface area, and Euler–Poincaré characteristic between the training and synthetic datasets agree well and have similar margins of error. The second-order functional, represented as the mean breadth, between the two datasets are not in agreement, suggesting some differences in the curvature of the generated dataset. For single-phase flow in an isotropic sandstone, the surface-to-volume ratio and topology, represented by the specific surface area and Euler–Poincaré characteristic, respectively, largely affects flow behavior (Mecke and Arns, 2005). However, for multiphase flow of oil and gas in more complex microporous systems,

matching the curvature becomes important in order to capture the curved interfaces between the immiscible phases.

### 5.3. Petrophysics

Fig. 7 shows the effective porosity and permeability relationship for 10 to 20 samples of the training and synthetic volumes. The effective porosity is used because the fluid only flows through the connected pore space. It is determined by calculating the number of grid cells assigned to the pore space and dividing by the total grid cells in the mesh. We observe good agreement between the original and synthetic systems in terms of the porosity–permeability relationship, using both Navier–Stokes and LBM calculations. The shift in porosity between synthetic and experimental curves is about 4% that is quite limited.

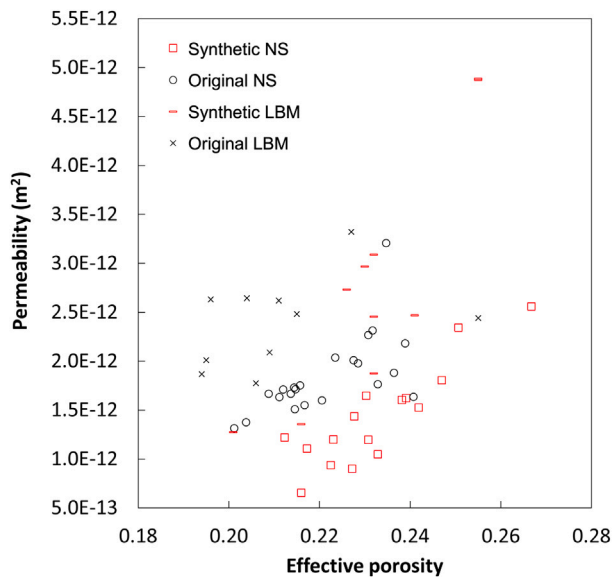


Fig. 7. Single-phase permeability and the corresponding effective porosity for multiple realizations of the sandstone training dataset and generated synthetic images. Permeability is computed via Navier–Stokes (NS) or LBM methods, as detailed in the legend.

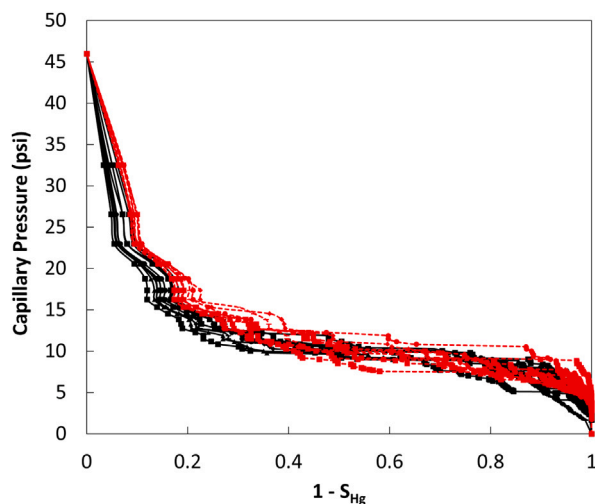


Fig. 8. Capillary pressure vs. mercury saturation, modeled as drainage along the vertical axis with a constant contact angle for original (black) and synthetic (red) pore volumes. (For interpretation of the references to color in this figure legend, the reader is referred to the web version of this article.)

Figs. 8 and 9 shows the mercury intrusion porosimetry and pore-size distribution curves for the training and synthetic volumes. There is very little variability in the synthetic volumes. From the MICP graph, we observe that the synthetic dataset has a greater frequency of large pores compared to the original dataset. Given the sensitivity of MICP calculations to small changes in grain shape as well as the edge effects observed from the covariance curves (Fig. 5), the difference is reasonable. The overall PSD and trend of the drainage experiment between the original and synthetic volumes show good agreement.

From Fig. 9, we also note that the pore-size distribution consists primarily of smaller pores below 15 voxels ( $91.8\mu\text{m}$ ) with a few large pores in the synthetic and original volumes. The capillary pressure graph confirms the behavior and the percolating pore space (i.e. connected to both the top and the bottom) between the two datasets is similar.

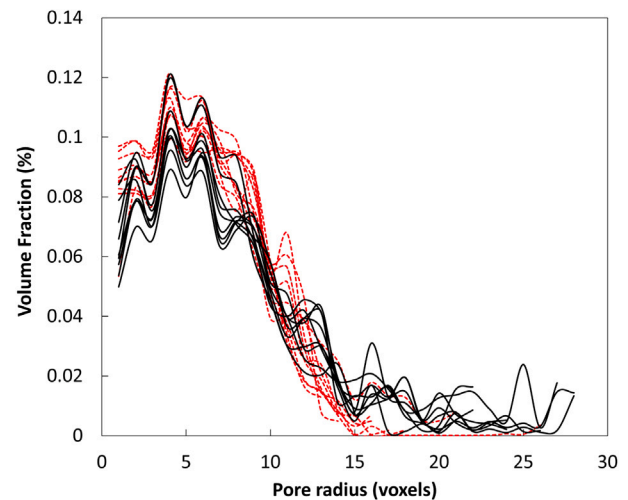


Fig. 9. Pore-size distribution for original (black) and synthetic (red) pore volumes. (For interpretation of the references to color in this figure legend, the reader is referred to the web version of this article.)

## 6. Discussion

The average chord length of the pore space, a statistical property, is useful to inform accurate 3D generation of a model trained on a 2D dataset. The agreement of the two-point correlation function and Minkowski functionals support this method. As shown in Fig. 4, step size has an important effect on the 3D statistical properties of the generated volume. The step size during interpolation refers to the number of intermediate images generated in between a pair of anchor slices. Deviations between the original and synthetic sample primarily occurred at small lag distances and demonstrate the difficulty of capturing the short-range properties in all directions. Deviations at larger lag distances may indicate over-fitting or that long-range properties were not completely captured during training. Small step sizes appear to match the long-range properties better, but exhibit periodic behavior that is not seen in the original sample.

Of the morphological metrics, we demonstrate excellent agreement between the porosity distribution of the original and synthetic datasets. The synthetic dataset is generated from a model that has no *a priori* knowledge of the target porosity, yet manages to recreate a grayscale volume that, when segmented, yields a comparable porosity. Given how many flow properties are correlated to porosity, the ability of the normalized flow model to match porosity provides further confidence in using these synthetic images for additional flow analysis.

One area for further study is the importance of matching the mean breadth, or integral of the mean curvature. This property has been shown to be highly sensitive to high-frequency features, such as noise and edges, and is difficult to estimate accurately (Arns et al., 2010; Legland et al., 2007; Wang et al., 2018). Other comparison metrics, specifically porosity, surface area, and Euler–Poincaré characteristic were sufficient to prove the accuracy of previously developed deep-learning models (Mosser et al., 2017; Alanov et al., 2020).

The agreement between the computed permeability of the original and synthetic datasets demonstrates the feasibility of using a normalized flow-based method to generate 3D volumes to understand uncertainty in petrophysical parameters. Both OpenFOAM and LBM methods used to compute permeability led to similar agreement between the permeability–porosity relationship of the synthetic and original pore volumes. Comparing the two methods shows ease of using the generated volumes and scalability for LBM-type calculations versus a Navier–Stokes approach. The slight difference in the porosity and permeability relationship may be corrected by improving agreement

between the higher-order Minkowski functionals and is an area of further study.

Future areas of study involve investigating how the normalized flow model captures multi-scale and long-range behavior, and may be evaluated by comparing the two-point cluster function between the experimental and synthetic images (Jiao et al., 2009). It is possible to train on  $256 \times 256$  pixel images (or larger), but with a very limited batch size of 2 to 4 due to memory constraints. The model may also be used to generate more complex porous media, such as carbonate and shale volumes (Anderson et al., 2020a).

Understanding how 3D interpolation step size relates to the chord length or other statistical properties of these systems is an important extension, especially for systems with multi-scale properties of interest. The constant interpolation step size appears to correspond to spatially meaningful increments. These result in visible changes and periodic behavior in the spatial covariance of the sample when the step size is changed as shown in Fig. 5. These observations when combined with the pore chord length results suggest that the interpolation step should be related formally to statistical properties of the image dataset.

## 7. Conclusions

We developed and implemented a deep-learning method to generate rapidly 3D realizations of rock pore structure from 2D grayscale image slices of pore networks used as inputs into generative flow models. We apply the model to create volumes of a sandstone sample to demonstrate feasibility. The agreement of morphological and flow parameters confirm that the volumes created are realistic. The calculated pore properties, such as porosity, pore-size distribution, and permeability agree well with the physical sample and show an expected range of variance. The model training is able to scale efficiently with input image size, making it suitable for studying properties across multiple length scales, including the role of heterogeneity, without losing finer-grained features. During evaluation, the image slices are evaluated in parallel, allowing for  $\mathcal{O}(1)$  scaling for image volumes with arbitrarily large z-dimension.

We also investigated how step size during the interpolation of 3D space is tied to a statistical parameter, the two-point probability function. The calculated chord length is useful to estimate and optimize the step size value. The effect of step size on simulated morphological properties shows that statistical properties inform the generative model during the 3D interpolation step. The inclusion of a deep-learning based generation method with statistical information may allow for more accurate and fast generation of pore volumes. Further refinement of the interpolation process, however, is needed to improve agreement between simulated and measured higher-order morphological properties. The speed up obtained in volume generation is quite significant in comparison to generative adversarial networks without loss of representation, and even with an improvement in results.

## CRedit authorship contribution statement

**Kelly M. Guan:** Performed the NS flow calculations, Developed the image evaluation pipeline, assisted with development of the image synthesis algorithm by testing the algorithm across multiple datasets. **Timothy I. Anderson:** Developed and implemented the presented image volume synthesis algorithm. **Patrice Creux:** Provided the LBM, MICP, and PSD calculations and advised on the project. **Anthony R. Kovscek:** Acquired funding, conceptualized project, and supervised work.

## Declaration of competing interest

The authors declare that they have no known competing financial interests or personal relationships that could have appeared to influence the work reported in this paper.

**Table 2**

Acronyms and abbreviations.

Acronym	Definition
MPS	Multiple-Point Statistics
CCSIM	Cross-Correlation Based Simulation Method
MICP	Mercury Intrusion Capillary Pressure
PSD	Pore-Size Distribution
GAN	Generative Adversarial Network
DCGAN	Deep Convolutional GAN
CNN	Convolutional Neural Network
NS	Navier-Stokes
LBM	Lattice Boltzmann Method

## Code availability

Code for this paper was based on the work of Kingma and Dhariwal (2018). The algorithm is built upon the NICE and RealNVP generative models (Dinh et al., 2015, 2017). This implementation is entitled RockFlow V1.0. The code is open source under the MIT license and available at <https://github.com/supri-a/RockFlow>.

## Acknowledgments

This work was supported as part of the Center for Mechanistic Control of Water-Hydrocarbon-Rock Interactions in Unconventional and Tight Oil Formations (CMC-UF), an Energy Frontier Research Center funded by the U.S. Department of Energy, Office of Science, USA under DOE (BES) Award DE-SC0019165.

We thank Dassault Systèmes for providing computational resources for the LBM calculations. We thank the Stanford Center for Computational Earth & Environmental Sciences (CEES) for providing computational resources for the NS calculations. Part of this work was performed at the Stanford Nano Shared Facilities (SNSF), supported by the U.S. National Science Foundation, USA under award ECCS-1542152.

## Appendix. Nomenclature

See Table 2.

## References

- Alanov, A., Kochurov, M., Volkonskiy, D., Yashkov, D., Burnaev, E., Vetrov, D., 2020. User-controllable multi-texture synthesis with generative adversarial networks. In: VISIGRAPP 2020 - Proceedings of the 15th International Joint Conference on Computer Vision, Imaging and Computer Graphics Theory and Applications. 4, pp. 214–221. <https://doi.org/10.5220/0008924502140221>, arXiv:1904.04751.
- van Amersfoort, J., 2019. Glow-PyTorch. GitHub Repository. [GitHub, \url{https://github.com/y0ast/Glow-PyTorch}](https://github.com/y0ast/Glow-PyTorch).
- Anderson, T.I., Guan, K.M., Vega, B., Aryana, S., Kovscek, A.R., 2020a. Rockflow: Fast generation of synthetic source rock images using generative flow models. *Energies* submitted for publication.
- Anderson, T.I., Vega, B., Kovscek, A.R., 2020b. Multimodal imaging and machine learning to enhance microscope images of shale. *Comput. Geosci.* 145 (June), 104593. <https://doi.org/10.1016/j.cageo.2020.104593>.
- Arns, C.H., Knackstedt, M.A., Mecke, K., 2010. 3D structural analysis: Sensitivity of Minkowski functionals. *J. Microsc.* 240 (3), 181–196. <https://doi.org/10.1111/j.1365-2818.2010.03395.x>.
- Bai, T., Tahmasebi, P., 2020. Hybrid geological modeling: Combining machine learning and multiple-point statistics. *Comput. Geosci.* 142 (May), 104519. <https://doi.org/10.1016/j.cageo.2020.104519>.
- Barbosa, M., Maddess, T., Ahn, S., Chan-Ling, T., 2019. Novel morphometric analysis of higher order structure of human radial peri-papillary capillaries: relevance to retinal perfusion efficiency and age. *Sci. Rep.* 9 (1), 1–16. <https://doi.org/10.1038/s41598-019-49443-z>.
- Bear, J., 1972. Dynamics of Fluids in Porous Media. In: Dover Civil and Mechanical Engineering Series, Dover, <https://books.google.com/books?id=lurmlFGhtEC>.
- Caers, J., 2001. Geostatistical reservoir modelling using statistical pattern recognition. *J. Pet. Sci. Eng.* 29 (3–4), 177–188. [https://doi.org/10.1016/S0920-4105\(01\)00088-2](https://doi.org/10.1016/S0920-4105(01)00088-2).



- Callow, B., Falcon-Suarez, I., Marin-Moreno, H., Bull, J.M., Ahmed, S., 2020. Optimal X-ray micro-CT image based methods for porosity and permeability quantification in heterogeneous sandstones. *Geophys. J. Int.* 223 (2), 1210–1229. <https://doi.org/10.1093/gji/ggaa321>.
- Čapek, P., Hejtmánek, V., Brabec, L., Zikánová, A., Kočíř, M., 2009. Stochastic reconstruction of particulate media using simulated annealing: Improving pore connectivity. *Transp. Porous Media* 76 (2), 179–198. <https://doi.org/10.1007/s11242-008-9242-8>.
- Chan, S., Elsheikh, A.H., 2019. Parametric generation of conditional geological realizations using generative neural networks. *Comput. Geosci.* 23, 925–952.
- Chen, S., Kirubanandham, A., Chawla, N., Jiao, Y., 2016. Stochastic multi-scale reconstruction of 3D microstructure consisting of polycrystalline grains and second-phase particles from 2D micrographs. *Metall. Mater. Trans. A* 47 (3), 1440–1450. <https://doi.org/10.1007/s11661-015-3283-8>.
- Crouse, B., Freed, D.M., Koliha, N., Balasubramanian, G., Corp, E.X.A., Satti, R., Bale, D., 2016. A Lattice-Boltzmann Based Method Applied to Digital Rock Characterization of Perforation Tunnel Damage, In: International Symposium of the Society of Core Analysts, Snowmass, pp. 1–6.
- Dinh, L., Krueger, D., Bengio, Y., 2015. NICE: Non-linear independent components estimation, In: 3rd International Conference on Learning Representations, ICLR 2015 - Workshop Track Proceedings, (12), pp. 1–13, [arXiv:1410.8516](https://arxiv.org/abs/1410.8516).
- Dinh, L., Sohl-Dickstein, J., Bengio, S., 2017. Density estimation using real NVP, In: 5th International Conference on Learning Representations, ICLR 2017 - Conference Track Proceedings, [arXiv:1605.08803](https://arxiv.org/abs/1605.08803).
- Doube, M., Klosowski, M.M., Arganda-Carreras, I., Cordelières, F.P., Dougherty, R.P., Jackson, J.S., Schmid, B., Hutchinson, J.R., Shefelbine, S.J., 2010. BoneJ: Free and extensible bone image analysis in imageJ. *Bone* 47 (6), 1076–1079. <https://doi.org/10.1016/j.bone.2010.08.023>, <https://www.sciencedirect.com/science/article/pii/S8756328210014419>.
- Feng, J., He, X., Teng, Q., Ren, C., Chen, H., Li, Y., 2019. Reconstruction of porous media from extremely limited information using conditional generative adversarial networks. *Phys. Rev. E* 100 (3), 33308. <https://doi.org/10.1103/PhysRevE.100.033308>, [arXiv:1905.02135](https://arxiv.org/abs/1905.02135).
- Fokina, D., Muravleva, E., Ovchinnikov, G., Oseledets, I., 2020. Microstructure synthesis using style-based generative adversarial networks. *Phys. Rev. E* 101 (4), 43308. <https://doi.org/10.1103/PhysRevE.101.043308>, [arXiv:1909.07042](https://arxiv.org/abs/1909.07042).
- Fullwood, D.T., Kalidindi, S.R., Niezgoda, S.R., Fast, A., Hampson, N., 2008. Gradient-based microstructure reconstructions from distributions using fast fourier transforms. *Mater. Sci. Eng. A* 494 (1–2), 68–72. <https://doi.org/10.1016/j.msea.2007.10.087>.
- Goodfellow, I.J., Pouget-abadie, J., Mirza, M., Xu, B., Warde-farley, D., 2014. Generative-Adversarial-Nets. *Nips* 1–9. <https://doi.org/10.1017/CBO9781139058452>, [arXiv:1406.2661v1](https://arxiv.org/abs/1406.2661v1).
- Graves, A., 2013. Generating sequences with recurrent neural networks. pp. 1–43, [arXiv:1308.0850](https://arxiv.org/abs/1308.0850), [http://arxiv.org/abs/1308.0850](https://arxiv.org/abs/1308.0850).
- Guan, K.M., Nazarova, M., Guo, B., Tchelepi, H., Kovscek, A.R., Creux, P., 2019. Effects of image resolution on sandstone porosity and permeability as obtained from X-Ray microscopy. *Transp. Porous Media* 127 (1), 233–245. <https://doi.org/10.1007/s11242-018-1189-9>.
- Hochreiter, S., Schmidhuber, J., 1997. Long short-term memory. *Neural Comput.* 9 (8), 1735–1780. [https://doi.org/10.1007/978-1-4757-5388-2\\_2](https://doi.org/10.1007/978-1-4757-5388-2_2).
- Jiao, Y., Stillinger, F.H., Torquato, S., 2008. Modeling heterogeneous materials via two-point correlation functions. II. Algorithmic details and applications. *Phys. Rev. E* 77 (3), 1–15. <https://doi.org/10.1103/PhysRevE.77.031135>, [arXiv:0801.1314](https://arxiv.org/abs/0801.1314).
- Jiao, Y., Stillinger, F.H., Torquato, S., 2009. A superior descriptor of random textures and its predictive capacity. *Proc. Natl. Acad. Sci. USA* 106 (42), 17634–17639. <https://doi.org/10.1073/pnas.0905919106>, [arXiv:1201.0710](https://arxiv.org/abs/1201.0710).
- Josh, M., Esteban, L., Delle Piane, C., Sarout, J., Dewhurst, D.N., Clennell, M.B., 2012. Laboratory characterisation of shale properties. *J. Pet. Sci. Eng.* 88–89, 107–124. <https://doi.org/10.1016/j.petrol.2012.01.023>.
- Ketcham, R.A., Carlson, W.D., 2001. Acquisition, optimization and interpretation of x-ray computed tomographic imagery: Applications to the geosciences. *Comput. Geosci.* 27 (4), 381–400. [https://doi.org/10.1016/S0098-3004\(00\)00116-3](https://doi.org/10.1016/S0098-3004(00)00116-3).
- Kingma, D.P., Dhariwal, P., 2018. Glow: Generative flow with invertible  $1 \times 1$  convolutions. *Adv. Neural Inf. Process. Syst.* 2018-Decem, 10215–10224, [arXiv:1807.03039](https://arxiv.org/abs/1807.03039).
- Krutko, V., Belozorov, B., Budenny, S., Sadikhov, E., Kuzmina, O., Orlov, D., Muravleva, E., Koroteev, D., 2019. A new approach to clastic rocks pore-scale topology reconstruction based on automatic thin-section images and CT scans analysis. In: Proceedings - SPE Annual Technical Conference and Exhibition. 2019-Sept, <https://doi.org/10.2118/196183-ms>.
- Legland, D., Arganda-Carreras, I., Andrey, P., MorphoLibJ: integrated library and plugins for mathematical morphology with ImageJ, 10.1093/bioinformatics/btw413, [www.epfl.ch/sage/soft/watershed](https://www.epfl.ch/sage/soft/watershed).
- Legland, D., Kiéu, K., Devaux, M.F., 2007. Computation of Minkowski measures on 2D and 3D binary images. *Image Anal. Stereol.* 26 (2), 83–92. <https://doi.org/10.5566/ias.v26.p83-92>.
- Li, H., Chen, P.-E., Jiao, Y., 2018. Accurate reconstruction of porous materials via stochastic fusion of limited bimodal microstructural data. *Transp. Porous Media* 125 (1), 5–22. <https://doi.org/10.1007/s11242-017-0889-x>.
- Liu, X., Shapiro, V., 2015. Random heterogeneous materials via texture synthesis. *Comput. Mater. Sci.* 99, 177–189. <https://doi.org/10.1016/j.commatsci.2014.12.017>, <https://www.sciencedirect.com/science/article/pii/S0927025614008647>.
- Manwart, C., Torquato, S., Hilfer, R., 2000. Stochastic reconstruction of sandstones. *Phys. Rev. E* 62 (1 B), 893–899. <https://doi.org/10.1103/PhysRevE.62.893>.
- Mecke, K., Arns, C.H., 2005. Fluids in porous media: A morphometric approach. *J. Phys. Condensed Matter* 17 (9), <https://doi.org/10.1088/0953-8984/17/9/014>.
- Mosser, L., Dubrue, O., Blunt, M.J., 2017. Reconstruction of three-dimensional porous media using generative adversarial neural networks. *Phys. Rev. E* 96 (4), <https://doi.org/10.1103/PhysRevE.96.043309>, [arXiv:1704.03225](https://arxiv.org/abs/1704.03225).
- Mosser, L., Dubrue, O., Blunt, M.J., 2018. Conditioning of three-dimensional generative adversarial networks for pore and reservoir-scale models. pp. 1–5, [arXiv:1802.05622](https://arxiv.org/abs/1802.05622), [http://arxiv.org/abs/1802.05622](https://arxiv.org/abs/1802.05622).
- Mosser, L., Dubrue, O., Blunt, M.J., 2020. Stochastic seismic waveform inversion using generative adversarial networks as a geological prior. *Math. Geosci.* 52 (1), 53–79. <https://doi.org/10.1007/s11004-019-09832-6>, [arXiv:1806.03720](https://arxiv.org/abs/1806.03720).
- Osher, J., Schladtitz, K., 2009. 3D Images of Materials Structures: Processing and Analysis. Wiley, <https://books.google.com/books?id=50FAX1vIK64C>.
- Okabe, H., Blunt, M.J., 2004. Prediction of permeability for porous media reconstructed using multiple-point statistics. *Phys. Rev. E* 70 (6), 10. <https://doi.org/10.1103/PhysRevE.70.066135>.
- Okabe, H., Blunt, M.J., 2007. Pore space reconstruction of vuggy carbonates using microtomography and multiple-point statistics. *Water Resour. Res.* 43 (12), 3–7. <https://doi.org/10.1029/2006WR005680>.
- Pant, L.M., Berkeley, L., 2016. Stochastic characterization and reconstruction of porous media stochastic characterization and reconstruction of porous media by a thesis submitted in partial fulfillment of the requirements for the degree of doctor of philosophy department of mechanical. <https://doi.org/10.7939/R3WW7798B>.
- Papamakarios, G., Nalisnick, E., Rezende, D.J., Mohamed, S., Lakshminarayanan, B., 2019. Normalizing Flows for Probabilistic Modeling and Inference. pp. 1–60, [arXiv:1912.02762](https://arxiv.org/abs/1912.02762), [http://arxiv.org/abs/1912.02762](https://arxiv.org/abs/1912.02762).
- Radford, A., Metz, L., Chintala, S., 2015. Unsupervised Representation Learning with Deep Convolutional Generative Adversarial Networks. [arXiv:1511.06434](https://arxiv.org/abs/1511.06434), [http://arxiv.org/abs/1511.06434](https://arxiv.org/abs/1511.06434).
- Serra, J.P., Serra, J., Cressie, N.A.C., 1982. Image Analysis and Mathematical Morphology. In: Image Analysis and Mathematical Morphology, (v. 1), Academic Press, <https://books.google.com/books?id=RQIUAAIAAJ>.
- Tahmasebi, P., Hezarkhani, A., Sahimi, M., 2012. Multiple-point geostatistical modeling based on the cross-correlation functions. *Comput. Geosci.* 16 (3), 779–797. <https://doi.org/10.1007/s10596-012-9287-1>.
- Tahmasebi, P., Sahimi, M., Andrade, J.E., 2017. Image-based modeling of granular porous media. *Geophys. Res. Lett.* 44 (10), 4738–4746. <https://doi.org/10.1002/2017GL073938>.
- Tahmasebi, P., Sahimi, M., Caers, J., 2014. MS-CCSIM : Accelerating pattern-based geostatistical simulation of categorical variables using a multi-scale search in fourier space. *Comput. Geosci.* 67, 75–88. <https://doi.org/10.1016/j.cageo.2014.03.009>.
- Torquato, S., 2005. Random Heterogeneous Materials: Microstructure and Macroscopic Properties. In: Interdisciplinary Applied Mathematics, Springer New York, [https://books.google.com/books?id=PhG\\_{X}4-8DPAC](https://books.google.com/books?id=PhG_{X}4-8DPAC).
- Uzunova, H., Ehrhardt, J., Jacob, F., Frydrychowicz, A., Handels, H., 2019. Multi-scale GANs for memory-efficient generation of high resolution medical images. [arXiv:1907.01376](https://arxiv.org/abs/1907.01376), [http://arxiv.org/abs/1907.01376](https://arxiv.org/abs/1907.01376).
- Volkonskiy, D., Muravleva, E., Sudakov, O., Orlov, D., Krutko, V., Burnaev, E., Koroteev, D., 2019. Reconstruction of 3D porous media from 2D slices. pp. 75–79, [arXiv:1901.10233v3](https://arxiv.org/abs/1901.10233v3).
- Walsh, J.B., Frangos, W.T., 1968. Permeability of granite under high pressure. *J. Geophys. Res.* 73 (6).
- Wang, Y.D., Armstrong, R.T., Mostaghimi, P., 2020. Boosting resolution and recovering texture of 2D and 3D Micro-CT images with deep learning. *Water Resour. Res.* 56 (1), 1–21. <https://doi.org/10.1029/2019WR026052>.
- Wang, Y., Arns, C.H., Rahman, S.S., Arns, J.Y., 2018. Porous structure reconstruction using convolutional neural networks. *Math. Geosci.* 1–19. <https://doi.org/10.1007/s11004-018-9743-0>, [arXiv:1609.01000v1](https://arxiv.org/abs/1609.01000v1).
- Wang, Y., Aryana, S.A., 2020. Journal of natural gas science and engineering pore-scale simulation of gas flow in microscopic permeable media with complex geometries. *J. Natural Gas Sci. Eng.* 81 (June), 103441. <https://doi.org/10.1016/j.jngse.2020.103441>.
- Washburn, E.W., 1921. The dynamics of capillary flow. *Phys. Rev.* 17 (3), 273–283. <https://doi.org/10.1103/PhysRev.17.273>, [arXiv:1011.1669v3](https://arxiv.org/abs/1011.1669v3).

- Weller, H.G., Tabor, G., Jasak, H., Fureby, C., 1998. A tensorial approach to computational continuum mechanics using object-oriented techniques. *Comput. Phys.* 12 (6), 620. <https://doi.org/10.1063/1.168744>, <https://aip.scitation.org/doi/abs/10.1063/1.168744>.
- Whitaker, S., 1986. Flow in porous media I: A theoretical derivation of Darcy's law. *Transp. Porous Media* 1 (1), 3–25. <https://doi.org/10.1007/BF01036523>, <http://link.springer.com/10.1007/BF01036523>.
- Yeong, C.L.Y., Torquato, S., 1998. Reconstructing random media. II. Three-dimensional media from two-dimensional cuts. *Phys. Rev. E* 58, 224–233. <https://doi.org/10.1103/PhysRevE.58.224>, <https://link.aps.org/doi/10.1103/PhysRevE.58.224>.
- Zhu, J.Y., Park, T., Isola, P., Efros, A.A., 2017. Unpaired image-to-image translation using cycle-consistent adversarial networks. In: *Proceedings of the IEEE International Conference on Computer Vision*. 2017-Oct, pp. 2242–2251. <https://doi.org/10.1109/ICCV.2017.244>, arXiv:1703.10593.